



ARL-TR-8082 • Aug 2017

**ARL**

US Army Research Laboratory

# Experimental Flight Characterization of Spin-Stabilized Projectiles at High Angle of Attack

by Frank Fresconi and Ilmars Celmins

Approved for public release; distribution is unlimited.

## **NOTICES**

### **Disclaimers**

The findings in this report are not to be construed as an official Department of the Army position unless so designated by other authorized documents.

Citation of manufacturer's or trade names does not constitute an official endorsement or approval of the use thereof.

Destroy this report when it is no longer needed. Do not return it to the originator.



# Experimental Flight Characterization of Spin-Stabilized Projectiles at High Angle of Attack

by Frank Fresconi and Ilmars Celmins

*Weapons and Materials Research Directorate, ARL*

## REPORT DOCUMENTATION PAGE

*Form Approved*  
OMB No. 0704-0188

Public reporting burden for this collection of information is estimated to average 1 hour per response, including the time for reviewing instructions, searching existing data sources, gathering and maintaining the data needed, and completing and reviewing the collection information. Send comments regarding this burden estimate or any other aspect of this collection of information, including suggestions for reducing the burden, to Department of Defense, Washington Headquarters Services, Directorate for Information Operations and Reports (0704-0188), 1215 Jefferson Davis Highway, Suite 1204, Arlington, VA 22202-4302. Respondents should be aware that notwithstanding any other provision of law, no person shall be subject to any penalty for failing to comply with a collection of information if it does not display a currently valid OMB control number.

**PLEASE DO NOT RETURN YOUR FORM TO THE ABOVE ADDRESS.**

1. REPORT DATE (DD-MM-YYYY) August 2017			2. REPORT TYPE Technical Report		3. DATES COVERED (From - To) June 2016–June 2017	
4. TITLE AND SUBTITLE Experimental Flight Characterization of Spin-Stabilized Projectiles at High Angle of Attack					5a. CONTRACT NUMBER	
					5b. GRANT NUMBER	
					5c. PROGRAM ELEMENT NUMBER	
6. AUTHOR(S) Frank Fresconi and Ilmars Celmins					5d. PROJECT NUMBER AH80	
					5e. TASK NUMBER	
					5f. WORK UNIT NUMBER	
7. PERFORMING ORGANIZATION NAME(S) AND ADDRESS(ES) US Army Research Laboratory Weapons and Materials Research Directorate ATTN: RDRL-WML-E Aberdeen Proving Ground, MD 21005-5066					8. PERFORMING ORGANIZATION REPORT NUMBER  ARL-TR-8082	
9. SPONSORING/MONITORING AGENCY NAME(S) AND ADDRESS(ES)					10. SPONSOR/MONITOR'S ACRONYM(S)	
					11. SPONSOR/MONITOR'S REPORT NUMBER(S)	
12. DISTRIBUTION/AVAILABILITY STATEMENT Approved for public release; distribution is unlimited.						
13. SUPPLEMENTARY NOTES						
14. ABSTRACT The goal of this study was to better understand the flight of spin-stabilized projectiles at high angle of attack for improved delivery accuracy of indirect fires. Experiments successfully captured flight motions over 40° angle of attack around Mach 0.8 using advanced spark range techniques. Flight analysis validated analytical expressions, kinematics, and dynamics with mass asymmetries, aerodynamic modeling, and parameter estimation algorithms. Significant nonlinearities in angle of attack were quantified in the axial force and Magnus moment with more-linear behavior found in the normal force and pitching moment. Stability analysis indicated that this vehicle does not fly below 3° angle of attack and likely suffers instabilities around 3° angle of attack. These results ultimately improve impact point prediction for applications such as high-arcing, spin-stabilized munitions.						
15. SUBJECT TERMS aerodynamics, spark range, spin-stabilized projectile, high angle of attack, parameter estimation						
16. SECURITY CLASSIFICATION OF:			17. LIMITATION OF ABSTRACT  UU	18. NUMBER OF PAGES  36	19a. NAME OF RESPONSIBLE PERSON Frank Fresconi	
a. REPORT Unclassified	b. ABSTRACT Unclassified	c. THIS PAGE Unclassified			19b. TELEPHONE NUMBER (Include area code) 410-306-0794	

Standard Form 298 (Rev. 8/98)  
Prescribed by ANSI Std. Z39.18

## Contents

---

List of Figures	iv
List of Tables	iv
Acknowledgments	v
1. Introduction	1
2. Flight Modeling	2
3. Spark Range Firings	3
4. Parameter Estimation Algorithm	5
5. Results	6
6. Conclusions	20
7. References	22
Distribution List	25

## List of Figures

---

---

Fig. 1	Flight follower of spin-stabilized vehicle flying to approximately 25° angle of attack.....	5
Fig. 2	Orthogonal shadowgraphs .....	7
Fig. 3	Center-of-gravity motion .....	8
Fig. 4	Roll motion .....	9
Fig. 5	Angular motion .....	9
Fig. 6	Fixed-plane angular motion .....	10
Fig. 7	Relationship between internal mass orientation and swerve direction .....	11
Fig. 8	Summary flight motion .....	12
Fig. 9	Summary angle of attack histories .....	13
Fig. 10	Relationship between maximum total angle of attack and tilt axis ....	14
Fig. 11	Axial force coefficient .....	15
Fig. 12	Static normal force coefficient.....	16
Fig. 13	Static pitching moment coefficient .....	17
Fig. 14	Pitch and roll damping moment coefficients .....	18
Fig. 15	Magnus moment coefficient .....	19

## List of Tables

---

---

Table 1	Mass properties of flight vehicles .....	4
---------	--	---

## Acknowledgments

---

The authors appreciate the contributions of Bernard Guidos (US Army Research Laboratory [ARL]); the crew of the Transonic Experimental Facility, John Heath (ARL), Barry Hudler (ARL), Ken Willan (ARL), Eric Miller (ARL), Bill Aubry (ARL), and Jarid Kranz (ARL); Bobby Hall (ARL) and the machinists at the Weapons and Materials Directorate machine shop; Jeff Damiano (Aberdeen Test Center); Ron Anderson (ARL); Andrew Brant (ARL); and Wayne Hathaway (Arrow Tech Associates).

INTENTIONALLY LEFT BLANK.

# 1. Introduction

---

The motivation for this study is to better understand the high-angle-of-attack flight behavior of spin-stabilized projectiles. Gyroscopically stabilized projectiles launched at steep angles for indirect fire experience large yaw of repose in the subsonic regime. The uncertainties associated with the aerodynamics at these high angles of attack increase the delivery error due to poor fire-control solutions (i.e., understanding the relationship between the gun pointing angle and the impact location). Guidance kits emplaced on these spin-stabilized vehicles can also induce significant angle of attack to maneuver. Accurate characterization of these aerodynamics is critical to removing miss distance, especially since control authority is often limited in these applications.

Guns are rifled to impart spin to projectiles, which can improve delivery accuracy and lower velocity decay over aerodynamically stabilized projectiles. The overwhelming majority of spin-stabilized projectiles undergo motion solely due to the external forces and moments of gravity and rigid aerodynamic surfaces (i.e., flight is not controlled by actuating moveable aerodynamic surfaces). The angle of attack in these applications is usually below  $10^\circ$ . For this reason, the literature on spin-stabilized projectile aerodynamics has focused on lower angles of attack. High angle of attack will be defined for the purposes of this study to be over  $10^\circ$ . While static aerodynamics (e.g., drag force, lift force, and overturning moment) are important to spin-stabilized flight, the rate-dependent aerodynamics (e.g., pitch damping moment, Magnus moment, and roll damping moment) are also critical due to the role these phenomena play in ballistic flight stability.<sup>1</sup> Wind tunnel techniques have been employed using spinning models<sup>2-5</sup> to directly measure forces and moments but suffer from typical sting and wall interference effects and encounter difficulties determining dynamic aerodynamic coefficients. The spark range,<sup>6-8</sup> onboard sensor,<sup>9-13</sup> and high-speed video<sup>14</sup> techniques have no sting or wall effects since the vehicle is in free flight. These techniques provide good dynamic aerodynamics but do not directly measure forces and moments and feature limited control over the angle of attack range. Computational fluid dynamics techniques<sup>15-20</sup> have enjoyed increasing success when applied to spin-stabilized projectile aerodynamics over the past 35 years.

The contributions of the present work include defining the state of the art in experimental flight techniques and improving the understanding of nonlinearities in the aerodynamics of spin-stabilized projectiles. To accomplish this, nonlinear and linear flight models were formulated with the appropriate aerodynamic models. Experiments were designed and executed to capture accurate data on models flying at high subsonic to low transonic speeds with varying degrees of angle of attack

from very low ( $\sim 0^\circ$ ) to very high ( $\sim 40^\circ$ ) using repeatable yaw induction techniques.<sup>21</sup> Parameter estimation algorithms were applied that resulted in residuals on the order of the measurement errors and subsequently provided the angle-of-attack dependency in the aerodynamic coefficients. These experiments validated the modeling and data analysis approach and ultimately provide insight into how to improve delivery accuracy of spin-stabilized projectiles flying at high angle of attack.

## 2. Flight Modeling

The flight modeling approach in this study seeks the simplest form that represents the relevant phenomenon. The following equations govern the flight motion of gyroscopically stabilized vehicles and can be found in the literature.<sup>1,22</sup> The rigid-body kinematics (Eqs. 1 and 2) and dynamics (Eqs. 3 and 4) are obtained straightforwardly from considering first principles. The rotational dynamics expressions used in this study (Eq. 4) are somewhat complicated by the inclusion of asymmetric mass configurations in experiments.

$$\begin{bmatrix} \dot{x} \\ \dot{y} \\ \dot{z} \end{bmatrix} = \begin{bmatrix} c_\theta c_\psi & s_\phi s_\theta c_\psi - c_\phi s_\psi & c_\phi s_\theta c_\psi + s_\phi s_\psi \\ c_\theta s_\psi & s_\phi s_\theta s_\psi + c_\phi c_\psi & c_\phi s_\theta s_\psi + s_\phi c_\psi \\ -s_\theta & s_\phi c_\theta & c_\phi c_\theta \end{bmatrix} \begin{bmatrix} u \\ v \\ w \end{bmatrix}. \quad (1)$$

$$\begin{bmatrix} \dot{\phi} \\ \dot{\theta} \\ \dot{\psi} \end{bmatrix} = \begin{bmatrix} 1 & s_\phi t_\theta & c_\phi t_\theta \\ 0 & c_\phi & -s_\phi \\ 0 & s_\phi/c_\theta & c_\phi/c_\theta \end{bmatrix} \begin{bmatrix} p \\ q \\ r \end{bmatrix}. \quad (2)$$

$$\begin{bmatrix} \dot{\phi} \\ \dot{\theta} \\ \dot{\psi} \end{bmatrix} = \begin{bmatrix} 1 & s_\phi t_\theta & c_\phi t_\theta \\ 0 & c_\phi & -s_\phi \\ 0 & s_\phi/c_\theta & c_\phi/c_\theta \end{bmatrix} \begin{bmatrix} p \\ q \\ r \end{bmatrix}. \quad (3)$$

$$\begin{bmatrix} \dot{p} \\ \dot{q} \\ \dot{r} \end{bmatrix} = \begin{bmatrix} I_{XX} & I_{XY} & I_{XZ} \\ I_{XY} & I_{YY} & I_{YZ} \\ I_{XZ} & I_{YZ} & I_{ZZ} \end{bmatrix}^{-1} \begin{bmatrix} L + Z(CG_{Y,N} - CG_{Y,R})D - Y(CG_{Z,N} - CG_{Z,R})D \\ M + X(CG_{Z,N} - CG_{Z,R})D - Z(CG_{X,N} - CG_{X,R})D \\ N + Y(CG_{X,N} - CG_{X,R})D - X(CG_{Y,N} - CG_{Y,R})D \end{bmatrix} - \begin{bmatrix} I_{XX} & I_{XY} & I_{XZ} \\ I_{XY} & I_{YY} & I_{YZ} \\ I_{XZ} & I_{YZ} & I_{ZZ} \end{bmatrix}^{-1} \begin{bmatrix} 0 & -r & q \\ r & 0 & -p \\ -q & p & 0 \end{bmatrix} \begin{bmatrix} I_{XX} & I_{XY} & I_{XZ} \\ I_{XY} & I_{YY} & I_{YZ} \\ I_{XZ} & I_{YZ} & I_{ZZ} \end{bmatrix} \begin{bmatrix} p \\ q \\ r \end{bmatrix}. \quad (4)$$

A more active area of research in flight modeling is the aerodynamic model (Eqs. 5–10), which is often configuration-dependent. The aerodynamic model used in this work includes nonlinearities in the static forces and moments, damping moments, and nonlinear Magnus (side) moments. Aerodynamic coefficients depend on Mach number and total angle of attack. Variation with aerodynamic roll angle is neglected (e.g., assume  $C_{n_\beta} = C_{m_\alpha}$ ) due to the configurational symmetry in the spin-stabilized vehicle shape. While polynomials are used for most

aerodynamic phenomena a table is implemented to capture the large nonlinearity in the Magnus moment with angle of attack.

$$X = -QS \left( C_{X_0} + C_{X_{\bar{\alpha}^2}} \sin^2 \bar{\alpha} \right). \quad (5)$$

$$Y = -QS \left( C_{N_\alpha} \sin \beta + C_{N_{\alpha^3}} \sin^3 \beta - C_{Y_{p\alpha}} \frac{pD}{2V} \sin \alpha \right). \quad (6)$$

$$Z = -QS \left( C_{N_\alpha} \sin \alpha + C_{N_{\alpha^3}} \sin^3 \alpha + C_{Y_{p\alpha}} \frac{pD}{2V} \sin \beta \right). \quad (7)$$

$$L = QSD C_{l_p} \frac{pD}{2V}. \quad (8)$$

$$M = QSD \left( C_{m_\alpha} \sin \alpha + C_{m_{\alpha^3}} \sin^3 \alpha + C_{m_q} \frac{qD}{2V} + C_{n_{p\alpha}} (\beta) \frac{pD}{2V} \sin \beta \right). \quad (9)$$

$$N = QSD \left( -C_{m_\alpha} \sin \beta - C_{m_{\alpha^3}} \sin^3 \beta + C_{m_q} \frac{rD}{2V} + C_{n_{p\alpha}} (\alpha) \frac{pD}{2V} \sin \alpha \right). \quad (10)$$

Multiple spark range flights in different angle of attack ranges yields the best information concerning the nonlinear aerodynamics. Various masses offset from the body axis of symmetry were placed within the projectiles to repeatably induce several magnitudes of yaw. Linearization of the flight motion<sup>1,22</sup> provides analytical relationships for the vehicle angular motion. This angular motion has components due to nutation, precession, and trims. Trims produce angular oscillations at the spin rate. Spin rate is given by gun rifling, launch velocity, axial moment of inertia, and roll damping moment for this application. The frequencies of nutation and precession can be obtained from the aerodynamics, mass properties, flight states, and atmospheric conditions, as given in Eq. 11.

$$\omega_{N,P} = \frac{pI_A}{2I_T V} \left[ 1 \pm \sqrt{1 - \frac{1}{\frac{2I_A^2 p^2}{\pi \rho I_T D^3 V^2 C_{m_\alpha}}}} \right]. \quad (11)$$

Equations relating the tilt angle (angle between the principal inertial axis and the body axis of symmetry) and the maximum total angle of attack<sup>23</sup> can be exploited for experiment design. Equation 12 was used to size different mass inserts for the projectiles during firings. The magnitude of the maximum total angle of attack increases significantly for high spin rates, which are usually encountered for gyroscopically stabilized applications.

$$\bar{\alpha}_{MAX} = \left[ \frac{2p - \omega_N - \omega_P}{\omega_N - \omega_P} \right] \gamma. \quad (12)$$

### 3. Spark Range Firings

---

Fifteen vehicles were flown through the spark range with 7 different mass insert configurations. The mass properties were obtained using a special procedure crafted to determine the full moment of inertia tensor on precision measurement

devices. Mass properties of the vehicles are provided in Table 1. The tilt axis is related to the moments of inertia ( $I_{XY} = \frac{I_{YY} - I_{XX}}{2} \tan 2\gamma$ ). The external shape of the projectile was characteristic of an artillery application.

**Table 1** Mass properties of flight vehicles

No. of Flights	Mass (kg)	Longitudinal center of gravity <sup>a</sup> (mm)	Lateral center of gravity <sup>a</sup> (mm)	Axial inertia (kg-m <sup>2</sup> )	Trans. inertia (kg-m <sup>2</sup> )	Cross-axis inertia (kg-m <sup>2</sup> )
2	25.3921	0.559499	0	0.114429	1.166983	0
1	26.8250	0.571576	0.001016	0.116729	1.311924	0.001835
4	27.3153	0.575840	0.000787	0.117523	1.311924	0.007454
1	27.9322	0.578321	0.001886	0.119091	1.311924	0.008985
1	28.2588	0.580697	0.002273	0.119250	1.311924	0.011786
4	28.8394	0.582118	0.003000	0.120505	1.318907	0.012992
2	29.2658	0.587317	0.004114	0.120707	1.370948	0.019349

<sup>a</sup> From nose

A 155-mm-diameter rifled gun launched the vehicles. A half muzzle break was not used to induce yaw in an attempt to isolate angular motion due to asymmetric mass. The gun was mounted in a tracked vehicle and positioned with the muzzle about 2 m from the spark range entrance. The propelling charge used 1.18 kg of M1 propellant with about 30 gr of black powder for the primer. These conditions resulted in launch speeds in the low transonic to high subsonic regime.

A series of preliminary firings were conducted with high-speed photography (fixed and flight follower using a rotating mirror), radar, yaw cards, and gun pressure gauges to establish the charge, verify structural integrity, assess flight stability, and validate the flight path prior to spark range firings. These firings were especially critical since the vehicles must fly through an approximately 2- × 2-m window at each station in the spark range. The gravity drop is significant at this Mach number, and the swerving motion is large for high-angle-of-attack experiments. A representative flight follower dataset on a configuration that reached about 25° angle of attack is provided in Fig. 1.



**Fig. 1 Flight follower of spin-stabilized vehicle flying to approximately 25° angle of attack**

The spark range technique has been applied with success over many years to study the flight behavior of different vehicle types such as aerodynamically stabilized projectiles (e.g., tank ammunition<sup>24</sup> and mortars), aircraft,<sup>6</sup> re-entry vehicles,<sup>25</sup> guided munitions,<sup>8,26</sup> as well as spin-stabilized projectiles.<sup>7</sup> The spark range at the US Army Research Laboratory's Transonic Experimental Facility<sup>27</sup> features 25 measurement stations in an enclosed building more than 250 m long. Each station is equipped with a light screen, delay unit, spark source, surveyed fiducials, and 2 orthogonal cameras for capturing shadowgraphs. As the vehicle flies past each station, the light screen triggers, which sets off the high-intensity, short-duration spark source after the appropriate delay to obtain the orthogonal shadowgraphs. Postprocessing of the shadowgraphs and trigger times yields the center-of-gravity location and Euler angles, which along with meteorological data are used to obtain aerodynamic coefficients in a parameter estimation algorithm.

#### **4. Parameter Estimation Algorithm**

---

The maximum likelihood method<sup>25,28,29</sup> was implemented to determine aerodynamics from these spark range firings. This is a nonlinear least-squares technique that seeks to find parameters that minimize a logarithmic function containing the residual between the experimental measurements and the model calculations. The parameter vector for this problem included the aerodynamic coefficients, initial conditions, and cross-axis moment of inertia. Magnus force was not included in the parameter estimation. The Magnus moment table was adjusted using linear and cubic terms (Eq. 13).

$$\Theta = \begin{bmatrix} C_{X_0} & C_{X_{\bar{\alpha}^2}} & C_{N_\alpha} & C_{N_{\alpha^3}} & C_{m_\alpha} & C_{m_{\alpha^3}} & C_{m_q} & C_{n_{p\alpha}} & C_{n_{p\alpha^3}} & C_{l_p} & I_{XY} & \dots \\ x_0 & y_0 & z_0 & \phi_0 & \theta_0 & \psi_0 & u_0 & v_0 & w_0 & p_0 & q_0 & r_0 \end{bmatrix}. \quad (13)$$

Initial guesses for these parameters were used to integrate both the nonlinear flight model (Eqs. 1–10) and differential equations for a Jacobian ( $\frac{\partial x_c}{\partial \Theta}$ ) to the end of the time series. A Newton-Raphson routine was applied to optimize the likelihood function at times containing experimental data. Equation 14 was used in this method to update the values in the parameter vector.

$$\Delta\Theta = \left( \sum_{i=1}^{N_M} \frac{\partial x_{c,i}^T}{\partial \Theta} \mathbb{R}^{-1} \frac{\partial x_{c,i}}{\partial \Theta} + \xi I \right)^{-1} \sum_{i=1}^{N_M} \frac{\partial x_{c,i}^T}{\partial \Theta} \mathbb{R}^{-1} \epsilon_i. \quad (14)$$

This procedure was iterated with the adjusted parameters until convergence was achieved.

## 5. Results

---

Representative shadowgraphs are provided in Fig. 2. These data were collected at the same instant in time in the horizontal (Fig. 2, bottom) and vertical (Fig. 2, top) planes. In each image the blurred shape is the actual vehicle, and the sharp shape is the shadow cast onto the panel by the spark source. At this station the vehicle is pitched up about 40° with a yaw angle near 0°. Note the pin inserted into the base to measure roll angle along with some wake flow structures trailing the body.

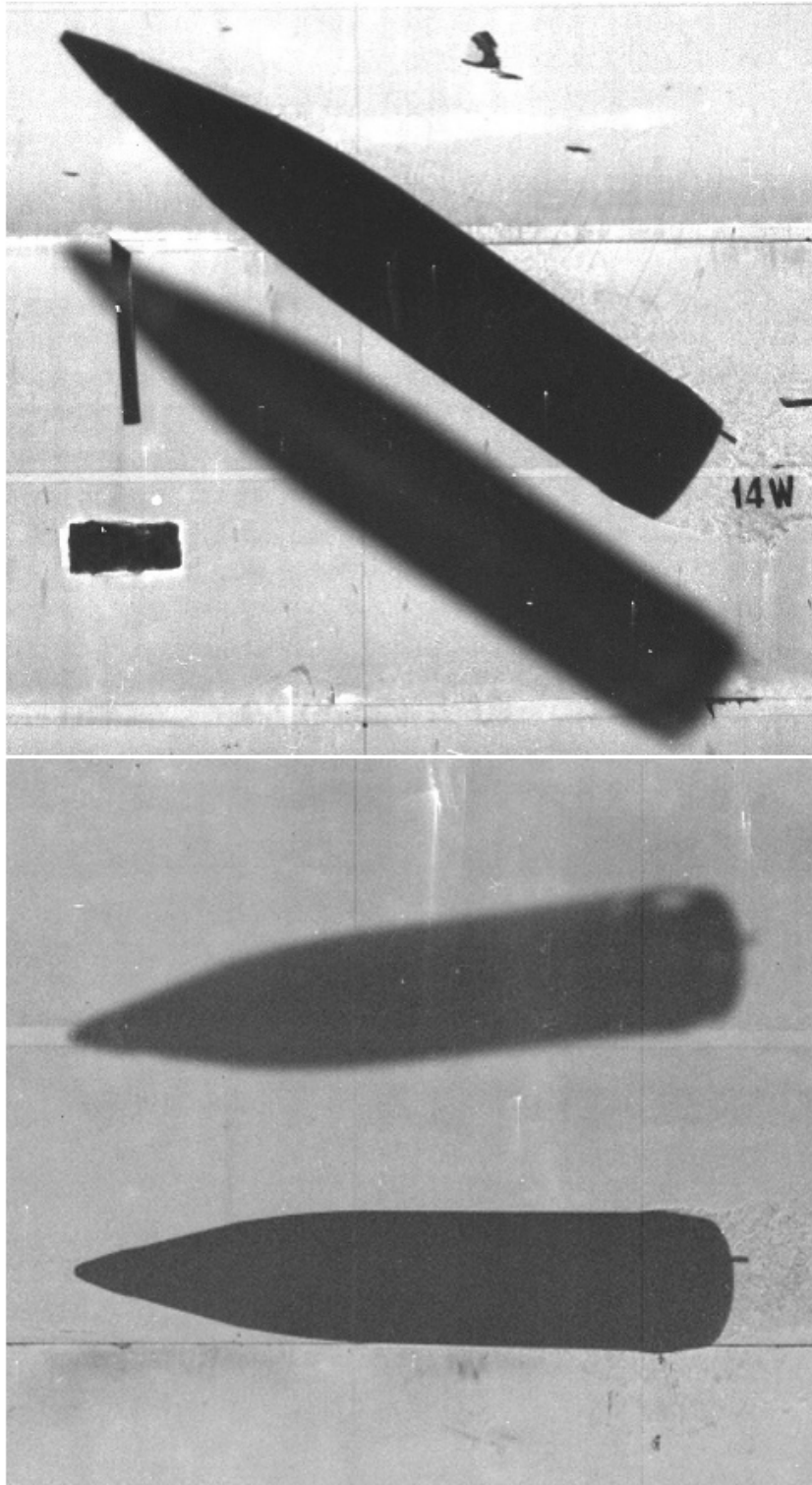


**Fig. 2 Orthogonal shadowgraphs**

Figures 3–6 show the measured and reconstructed motion for one of the flights. In these plots, the dots represent the experimental measurements and the curves represent the model calculations yielded by the parameter estimation algorithm. The horizontal and vertical center-of-gravity locations are illustrated in Fig. 3. The action of gravity is apparent in the data in the vertical plane. The horizontal data increase significantly with downrange location due to jump. This high-amplitude swerving motion is important because the accuracy in the estimated aerodynamic normal force increases with magnitude of the swerve. A swerving period (approximately 2 cycles in 200 m of downrange travel) is also evident in the horizontal data.

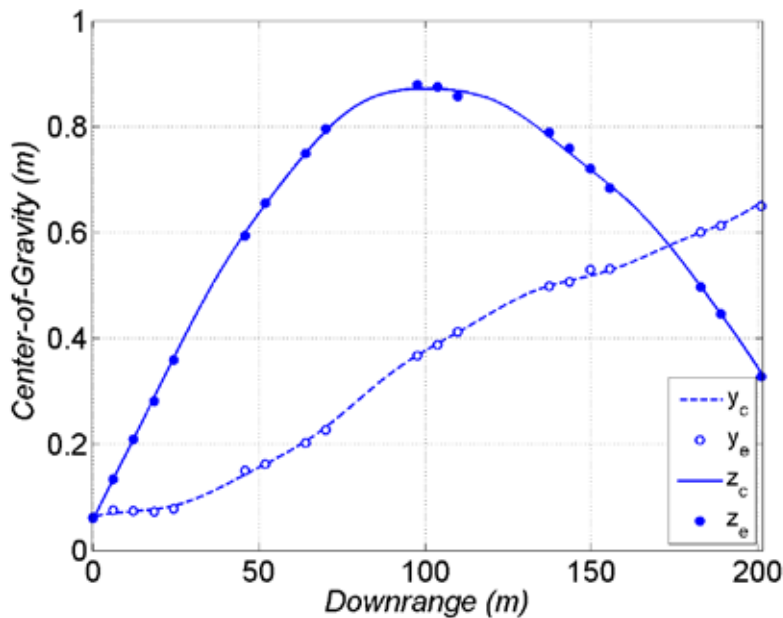
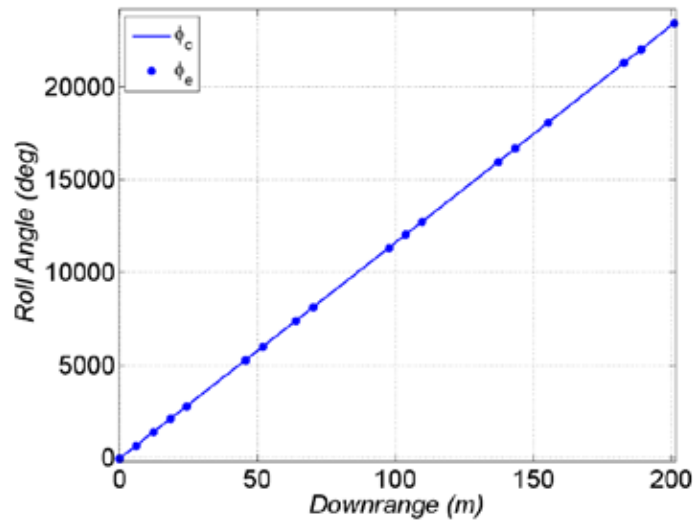


Fig. 3 Center-of-gravity motion

The rolling motion is captured in Fig. 4. These data are strongly linear with distance travelled because the launch spin rate is around 90 Hz and roll decelerates slightly due to aerodynamic damping. This vehicle rolls about 70 times over 200 m of downrange travel. For some of the high-angle-of-attack flights a significant amount of roll data were missing due to occlusions (i.e., the base prevented the pin from being in view), which limited the roll analysis. This was not problematic for the overall flight analysis because the roll motion is predictable for spin-stabilized projectiles flying these distances.



**Fig. 4 Roll motion**

The pitch and yaw motion for this flight is provided in Figs. 5 and 6. Figure 5 illustrates the tri-cyclic motion undergone by this vehicle. The nutation mode acts at the lowest frequency ( $\sim 2$  Hz), followed by the precession mode at a slightly higher frequency ( $\sim 6$  Hz), and finally the trim mode, which is at the spin rate ( $\sim 90$  Hz). Each of these modes is clearly visible by separate frequencies in the data. The data in Fig. 5 is plotted differently in Fig. 6 to show the complexity of this motion when viewed from the fixed-plane body reference and because this vehicle flies from about  $0^\circ$  to  $15^\circ$  total angle of attack. Collecting data over angle-of-attack ranges such as these is critical to investigating the nonlinear aerodynamics.

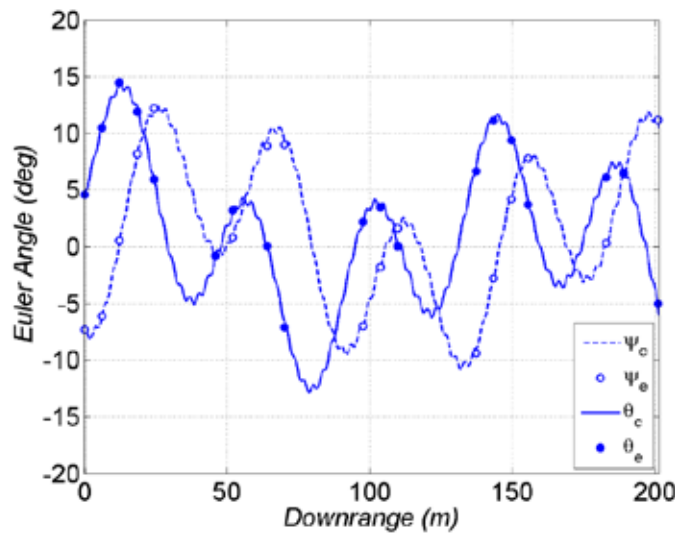


**Fig. 5 Angular motion**

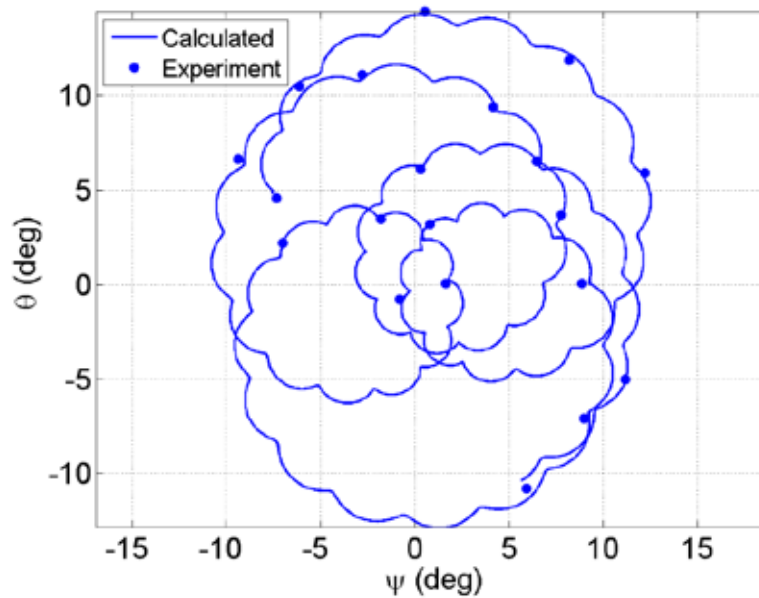


**Fig. 6 Fixed-plane angular motion**

Four firings of identical configurations with different initial roll orientations were conducted and data analysis performed to identify the relationship between the internal mass orientation and the swerve motion direction. These results are presented in Fig. 7. Each flight corresponds with a particular swerve direction (up, right, down, and left) as shown in the legend. The horizontal data given on the left of the figure is viewed from above looking toward the ground. The left flight horizontal position increases with downrange distance, and the right flight horizontal location decreases with downrange distance. The up and down flights remain approximately on the line of fire. The total span of swerve motion is approximately 1.5 m depending on the initial roll orientation. The oscillation in the swerve due to nutation and precession angular motion is apparent in the horizontal data. Inspection of the vertical data at the right of the figure shows a higher trajectory for the up flight and a lower trajectory for the down flight. The left flight is slightly higher than the right flight due to a higher launch elevation angle. The angle of attack histories for these flights with identical configurations was within about 20%, which indicates that this technique of using internal mass asymmetries for yaw induction is fairly repeatable.

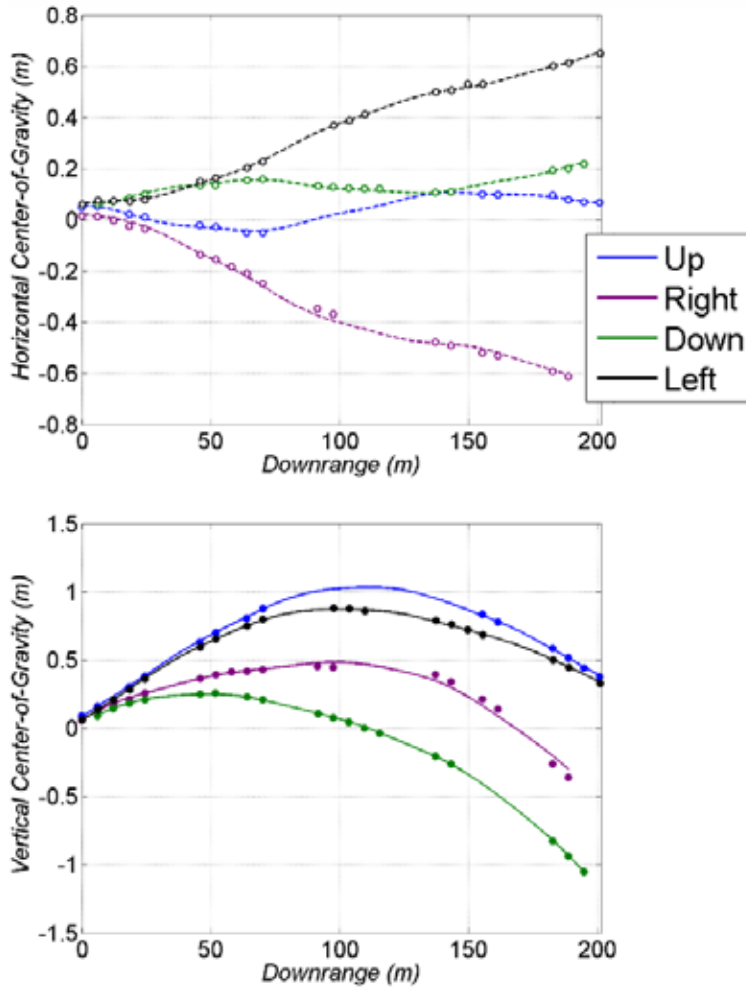


**Fig. 7 Relationship between internal mass orientation and swerve direction**

To obtain these swerve directions for spin-stabilized projectiles, the additional mass near the base must be  $90^\circ$  counter-clockwise (when viewed from the base) at launch from the desired swerve direction. As an example, if the desired swerve direction is up (i.e., 12:00) then at launch the mass insert near the base must be oriented to the left (i.e., 9:00) when viewed from behind the gun. Gun tube length, rifling, and load roll orientation must be known to prescribe the swerve direction in this manner.

The summary flight motion from all firings is provided in Fig. 8. The data were translated to better visualize the horizontal and vertical center of gravity. The spread in the horizontal and vertical center-of-gravity motion is about 2 m at 200 m downrange, which is about the size of the spark range instrumentation windows. This suggests that experiments were designed to maximize the observation of flight behaviors subject to experimental limitations. The Euler angles qualitatively show the relationship between angular motion amplitude and the tilt axis.

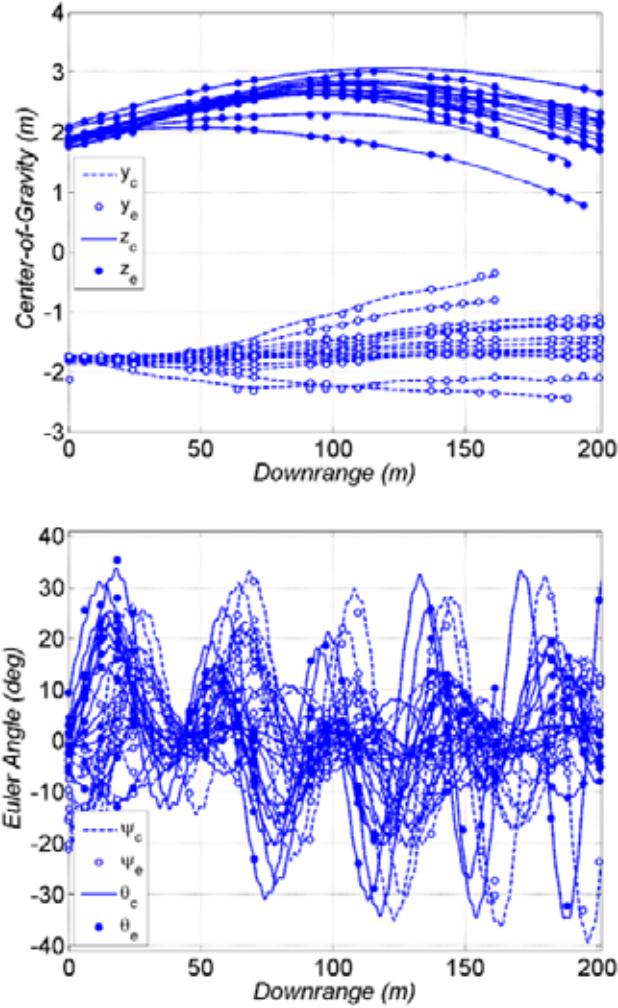


**Fig. 8 Summary flight motion**

Overall, the model matches the measurements to within the experimental error, which validates the aerodynamic model (Eqs. 5–10), kinematic and dynamic equations (Eqs. 1–4), and parameter estimation algorithm. There is larger uncertainty in the results at higher angle of attack. Measurement errors may be larger at higher angle of attack due to perspective changes of the camera/spark source and vehicle/shadowgraph. In addition, modeling errors may be larger due to neglecting nonlinear variation with angle of attack in the roll damping moment and pitch damping moment.

The total angle of attack histories for all flights are shown in Fig. 9. Experiments successfully captured a wide spectrum ( $0^\circ$ – $40^\circ$ ) of total angle of attack that is critical to examining nonlinearities in aerodynamics with angle of attack. Most flights appears stable; however, 2 of the flights at the largest angle of attack indicate growth in the angular motion amplitude with downrange distance. The oscillation

frequency in the angular motion is dictated primarily by the static pitching moment. The slight shifting in the frequencies of the angular motion illustrated in Fig. 9 is likely attributable to spread in the Mach histories of the flights in addition to potential variation in the static pitching moment with angle of attack and Mach number. The highest frequency in this data is at the spin rate due to the offset mass trim. The 2 lowest angle of attack flights do not exhibit this behavior due to the absence of an asymmetric mass for that configuration (see Table 1).

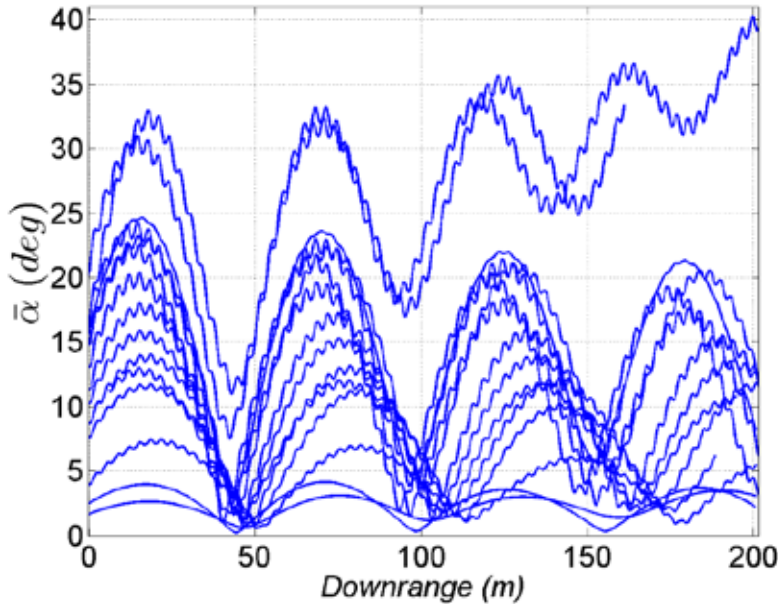


**Fig. 9** Summary angle of attack histories

The relationship between the maximum total angle of attack and the tilt axis obtained from this flight analysis and theory<sup>23</sup> (Eq. 12) is given in Fig. 10. The linear term in a least-squares fit to the experimental data is also shown. These results extend those shown by Rollstin and Hodapp<sup>12</sup> and imply that the analytical equation<sup>23</sup> is valid for designing experiments such as those conducted in this study.

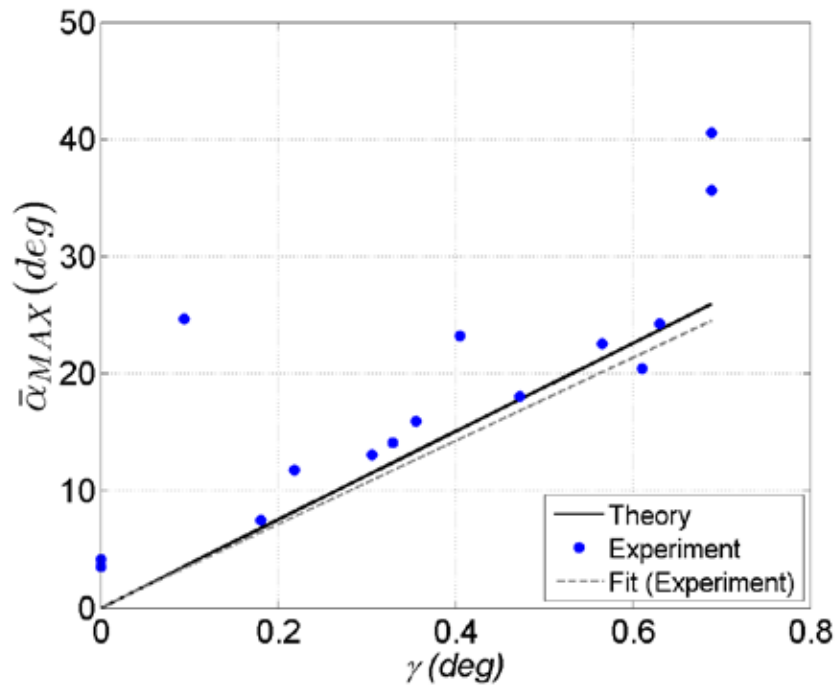


**Fig. 10 Relationship between maximum total angle of attack and tilt axis**

The aerodynamics that result from the flight analysis are presented next. The average Mach number for all flights was 0.77 with a standard deviation of 0.03. The moment reference location is 3.755 cal from the nose.

The axial force coefficient variation with angle of attack for individual flights and a least-squares fit to all the data is provided in Fig. 11. The zero-yaw axial force obtained in this study compares favorably with free-flight and wind tunnel results on similar spin-stabilized shapes and Mach numbers in Whyte<sup>7</sup> and Kahn et al.<sup>10</sup> Axial force increases approximately 70% from 0° to 25° total angle of attack. There is spread in the results at a particular aerodynamic angle. At small aerodynamic angles this scatter can be attributed to typical physical variations associated with manufacturing tolerances and the launch event.

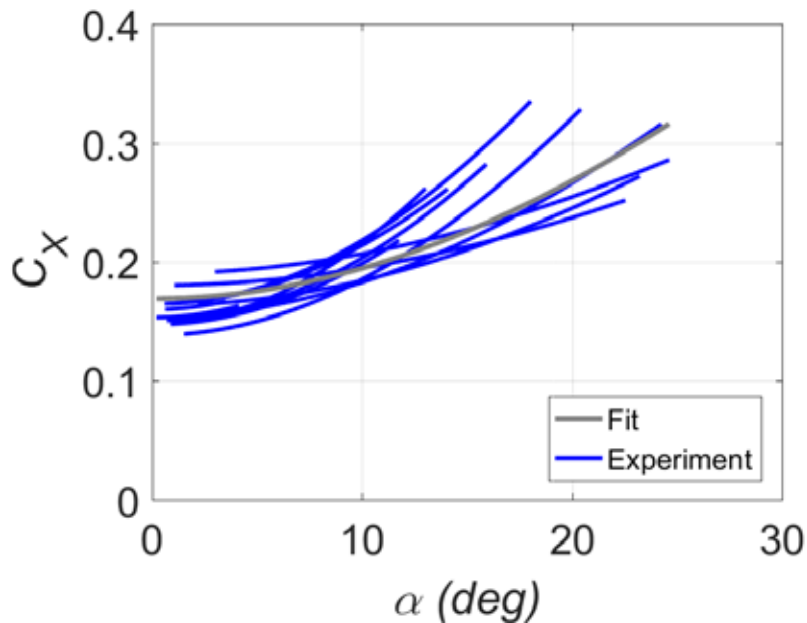


**Fig. 11 Axial force coefficient**

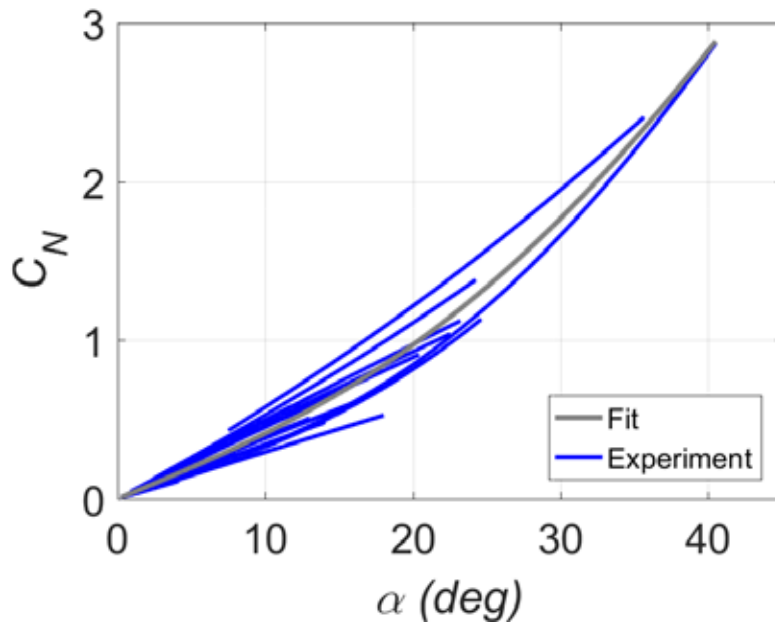
Spread in the data increases with aerodynamic angle, which indicates that a continuous polynomial does not represent the underlying flow phenomena at high angle of attack. There is little data in the literature on the axial force for spin-stabilized projectiles at high angle of attack on which to base a modeling approach. Flight analysis was conducted using a table (as done for the Magnus moment in this study) rather than a polynomial for the axial force aerodynamic model, but the results did not improve.

Obtaining accurate axial force at high angle of attack is challenging in these experiments for 2 primary reasons. First, aerodynamic forces and moments affect the accelerations of the vehicle, but the spark range measurements used for parameter estimation are positions (e.g., center-of-gravity location and Euler angles). Nonlinearities in the aerodynamics with angle of attack may be low-pass filtered as a result of integration from acceleration (i.e., aerodynamic force and moment) to position.

The second difficulty is related to the measurements for vehicles flying at high angle of attack. For typical spark range flights at low angle of attack, matching the time-stamped downrange center-of-gravity location provides the zero-yaw axial force. Matching the pitch and yaw angles permits assessment of the yaw component of axial force, which at low angle of attack is often small compared with the zero-yaw axial force. Matching the small swerve motion (primarily the horizontal and vertical center-of-gravity location) enables some evaluation of the normal force. In this situation the flight resembles a point-mass model. At high angle of attack the

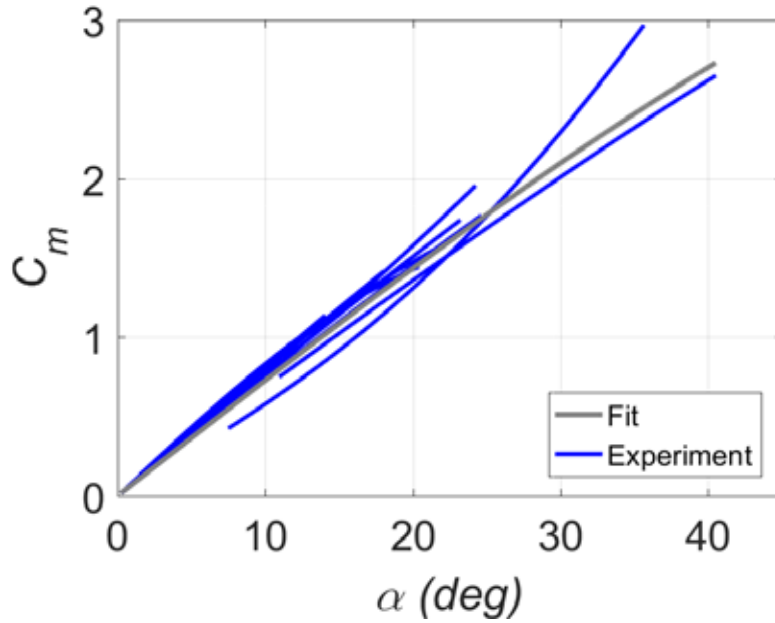
6-degree-of-freedom model is much more in play. Components of axial force as well as normal force contribute to the time-stamped downrange center-of-gravity location. Nonlinearities with angle of attack in the axial force and normal force are more important to matching the center-of-gravity measurements, so properly estimating the aerodynamic moments to match angular motion is extra critical. This situation increases the coupling between translational and rotational dynamics of the vehicle. In practice, for some of the highest angle-of-attack flights when the angular motion was well-fit by a set of aerodynamic moments, the axial force and normal force could be traded for an equivalent fit to the center-of-gravity motion. Moreover, the highest angle-of-attack flights were unstable, which was reflected in the numerical stability of the flight model and complicated the analysis.

Flying multiple identically shaped vehicles at a given Mach number over numerous angle-of-attack (including high) ranges arguably provides a “best” set of spark range data for obtaining aerodynamic normal force (i.e., high signal-to-noise ratio in lateral center-of-gravity motion data). These data are plotted in Fig. 12. The results suggest a mild (positive cubic term) nonlinearity with angle of attack up to 40°. Wind tunnel experiments with spinning models of similar geometry around Mach 0.3 also showed primarily linear behavior (small positive cubic term) in the normal force up to 70°, which were also largely independent of nondimensional spin rate.<sup>3</sup> The data in Fig. 12 also agree with relevant free-flight results by Whyte.<sup>7</sup>



**Fig. 12 Static normal force coefficient**

Figure 13 gives the static pitching moment coefficients. Similar to the normal force results, the static pitching moment is relatively linear (small negative cubic term) to 40°. These data agree with related experimental results presented by McCoy,<sup>3</sup> Whyte,<sup>7</sup> and Kahn et al.<sup>10</sup> McCoy<sup>3</sup> indicates an increased nonlinearity with angle of attack around 30°.



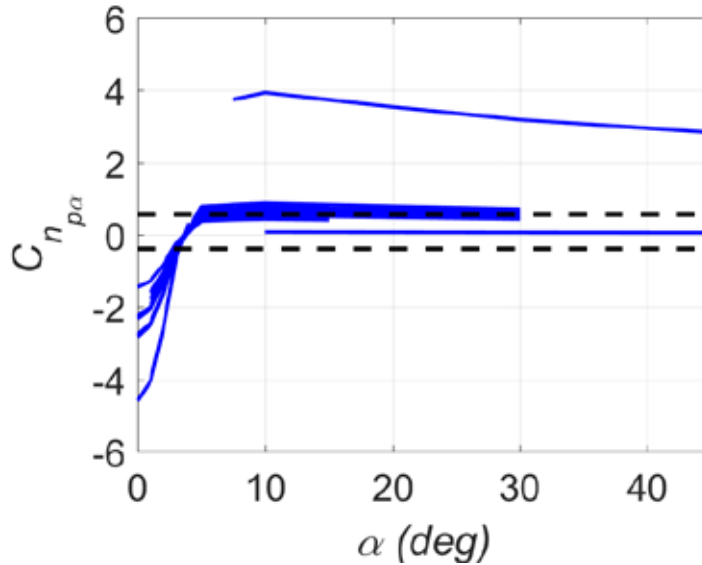
**Fig. 13 Static pitching moment coefficient**

Figure 14 provides the pitch damping moment (left) and roll damping moment (right) results as a function of the average Mach number of each flight since variation with angle of attack was neglected. The pitch damping moment features some scatter typical of spin-stabilized projectiles due to the ambiguity between pitch damping moment and Magnus moment from spark range observations explained elsewhere.<sup>1,30</sup> Pitch damping moments compare favorably with Whyte<sup>7</sup> and Kahn et al.<sup>10</sup>

Roll damping moment was obtained with some ease because the roll motion is relatively decoupled. There was some uncertainty, as described, due to occluded roll measurements, especially at high angle of attack. The roll damping moment results are repeatable and support those found by Whyte.<sup>7</sup>



in the Magnus moment at low angles because it is difficult to fly vehicles at very low angle of attack due to launch disturbances, internal and external vehicle asymmetries, and atmospheric effects such as wind. Combining this limited low angle of attack free-flight dataset and the current modeling approach yields a Magnus-induced nutation instability at small angles.



**Fig. 15 Magnus moment coefficient**

The increase in Magnus moment with angle of attack is supported in the literature on spinning bodies of revolution at subsonic Mach number.<sup>3,5,7,10</sup> Whyte<sup>5</sup> indicated a negative Magnus moment at low angles. McCoy<sup>3</sup> and Kahn et al.<sup>10</sup> were the only studies above 8° angle of attack. The nonlinearities in Magnus moment with angle of attack do not agree between these studies but that could be due to differences in Mach number or external shape. McCoy<sup>3</sup> observed large out-of-plane oscillations in spinning wind tunnel models for angle of attack between 30° and 150°. This phenomenon required averaging of the noisy gauge balance data and increased the uncertainty in the subsequent aerodynamic coefficients such as Magnus moments in this angle of attack range. Unsteady vortex shedding, similar to that found on slender bodies at high angle of attack<sup>31</sup> or long circular cylinders in a cross-flow (i.e., Karman vortex street), was offered to explain this behavior. Unsteady effects such as these were investigated by DeSpirito<sup>32</sup> and need further study to close gaps in understanding the interaction between the flow and the vehicle motion. Time-dependencies can be incorporated into the aerodynamic model (Eqs. 5–10)<sup>33</sup> at the appropriate aerodynamic angles to represent these phenomena.

## 6. Conclusions

---

This study was the first to characterize the aerodynamics of spin-stabilized vehicles in this Mach regime at high angle of attack from free-flight spark range data. The key findings and contributions to the state of the art are separated into 3 areas: experimental techniques, theory validation, and understanding of spin-stabilized vehicle flight behavior at high angle of attack.

Experiments were successful in demonstrating an approach for obtaining the desired high angle-of-attack flight behaviors while staying within spark range instrumentation windows. Vehicle physical characteristic modeling and measurements, preflight simulations, and preliminary firings with high-speed photography, radar, yaw cards, and gun pressure gauges were essential to designing the experiments and verifying the launch and flight system. Flights were repeatable, which enabled experiments to be performed up to  $40^\circ$  angle of attack. The consistency of results allowed the relationship between launch configuration roll orientation and swerve direction to be defined. Accurate raw data (e.g., asymmetric mass properties and shadowgraphs) were collected. Measurement errors due to the effect of perspective errors in the shadowgraph photography system at high angle of attack should be studied.

Theoretical expressions relating the vehicle tilt axis to the maximum total angle of attack were validated up to  $40^\circ$ . This lends credibility to applying these expressions for experimental design or performance analysis. Nonlinear stability theory should be explored further for spin-stabilized vehicles because linear stability bounds are inadequate at high angle of attack and do not provide suitable metrics. Flight analysis mainly achieved the expected measurement errors, which validates the kinematics and dynamics with internal asymmetries (Eqs. 1–4), aerodynamic modeling (Eqs. 5–10), and parameter estimation algorithms. This study revealed some limitations associated with obtaining aerodynamics from spark range flights. Nonlinearities in the aerodynamics with angle of attack are difficult to accurately assess because the aerodynamic forces and moments that appear in the acceleration equations can be low-pass filtered during analysis to the measurements of position. While some of these problems may be remedied with advanced parameter estimation algorithms and aerodynamic modeling, there are fundamental limitations associated with the measurement basis.

This study has extended the understanding of spin-stabilized vehicle flight in the high subsonic to low transonic Mach regime for high angle of attack. This knowledge can be applied to improve the accuracy of indirect fires for unguided (e.g., fire control) and guided (e.g., fire control, guidance and flight control algorithms) munitions launched at steep elevation angles that encounter high yaw

of repose. To improve prediction of the impact point under these conditions it is critical to accurately assess the axial force and normal force. The axial force dictates the decay of velocity and subsequent position history along the flight path. The normal force drives the drift of spin-stabilized projectiles (to the right from behind the gun) off the line of fire. This study indicates significant nonlinearity in axial force with angle of attack that may not be represented with a polynomial. Quantifying this nonlinearity and the underlying aerodynamic model structure are critical to impact point prediction. The results of this study suggest that normal force is relatively linear in angle of attack up to  $40^\circ$ , so devoting resources to quantify this aerodynamic coefficient at high angle of attack may not be as important as axial force.

The discussion of the relationship between the Magnus moment and stability underscored how spin-stabilized vehicles fly within a range of angle of attack. Extra effort should be taken in characterizing the aerodynamics across this angle-of-attack range. The Magnus moment, pitch damping moment, and static pitching moment primarily contribute to defining this angle-of-attack range. This study showed that for flat-fire trajectories (i.e., negligible yaw of repose) under nominal conditions, the angle-of-attack range is between about  $3^\circ$  and  $6^\circ$ . For steep elevation launch ( $\sim 70^\circ$ ) at high charge, the upper end of the angle-of-attack range can be as much as  $35^\circ$  due to yaw of repose (based on low angle-of-attack aerodynamics). The static pitching moment was mainly linear and the Magnus moment was highly nonlinear with angle of attack in this study. The pitch damping moment and roll damping moment were assumed independent of angle of attack in this work.

Overall, these results suggest that to improve delivery accuracy for spin-stabilized projectiles flying at high angle of attack due to steep elevation launch, it is of primary importance to quantify a set of highly nonlinear aerodynamics (axial force and Magnus moment) and of secondary importance to quantify a set of largely linear aerodynamics (normal force and static pitching moment) from about  $3^\circ$  to  $40^\circ$ . Recommendations for the pitch damping and roll damping moments are outside the scope of the present work but have been investigated by DeSpirito.<sup>32</sup>

## 7. References

---

---

1. Murphy CH. Free flight motion of symmetric projectiles. Aberdeen Proving Ground (MD): Army Ballistic Research Laboratories (US); 1963 July. Report No.: BRL-1216.
2. Platou AS. Magnus characteristics of finned and nonfinned projectiles. *AIAA J.* 1965;1(3).
3. McCoy RL. Subsonic aerodynamic characteristics of the 105 mm HE shell, M1 at angles of attack from zero to 180 degrees. Aberdeen Proving Ground (MD): Army Ballistic Research Laboratories (US); 1974 Mar. Report No.: BRL-MR-2353.
4. Miller M. Surface pressure measurements on a spinning wind tunnel model. *AIAA J.* 1976;14(12):1669–1670.
5. Oh S, Kim S, Lee D, Kim S, Ahn S. Magnus and spin-damping measurements of a spinning projectile using design of experiments. *J Spacecraft Rockets.* 2010;47(6):974–980.
6. Whyte RH, Winchenbach GL, Hathaway WH. Subsonic free-flight data for a complex asymmetric missile. *J Guid Cntrl Dyn.* 1981;4(1):59–65.
7. Whyte RH. Aerodynamic coefficients of the M483A1 determined from spark range tests. Aberdeen Proving Ground (MD): Army Ballistic Research Laboratories (US); 1991 Apr. Report No.: BRLCR-659.
8. Fresconi FE, Guidos B, Celmins I, DeSpirito J, Hathaway W. Flight behavior of an asymmetric missile through advanced characterization techniques. *J Spacecraft Rockets.* 2017;54(1):266–277.
9. Whyte RH, Mermagen WH. A method for obtaining aerodynamic coefficients from yawsonde and radar data. *J Spacecraft Rockets.* 1973;10(6):384–388.
10. Kahn SD, Oskay V, Whiteside J. Verification of ground test data by instrumented flight test of an artillery shell. *J Aircraft.* 1973;10(3):143–149.
11. Collings WZ, Lieske RF. Artillery shell drift at high angles of fire. *J Spacecraft Rockets.* 1975;12(3):169–173.
12. Rollstin SL, Hodapp AE. Experimental evaluation of artillery projectile impact errors induced by principal-axis misalignment. *J Spacecraft Rockets.* 1979;16(5):316–318.

13. Fresconi FE, Harkins T. Experimental flight characterization of asymmetric and maneuvering projectiles from elevated gun firings. *J Spacecraft Rockets*. 2012;49(6):1120–1130.
14. Decker RJ, Kolsch MN, Yakimenko OA. An automated method for computer vision analysis of cannon-launched projectile video. *J Test Eval*. 2015;42(5):1–9.
15. Nietubicz CJ, Pulliam TH, Steger JL. Numerical solution of the azimuthal-invariant thin-layer navier-stokes equations. *AIAA J*. 1980;18(12):1411–1412.
16. Sturek WB. Application of CFD to the aerodynamics of spinning shells. Reston (VA): American Institute of Aeronautics and Astronautics; 1984 Jan.
17. Sturek WB, Nietubicz CJ, Sahu J, Weinacht P. Applications of computational fluid dynamics to the aerodynamics of army projectiles. *J Spacecraft Rockets*. 1994;31(2):186–199.
18. Weinacht P. Projectile performance, stability, and free-flight motion prediction using computational fluid dynamics. *J Spacecraft Rockets*. 2004;41(2):257–263.
19. DeSpirito J, Silton S, Weinacht P. Navier-Stokes predictions of dynamic stability derivatives: evaluation of steady-state methods. *J Spacecraft Rockets*. 2009;46(6):1142–1154.
20. Sahu J. Computations of unsteady aerodynamics of a spinning body at transonic speeds. Reston (VA): American Institute of Aeronautics and Astronautics; 2009 Jun. AIAA Paper No.: 09-3852.
21. Davis B, Guidos B. A synopsis of yaw-induction techniques used during projectile free-flight aerodynamics experiments. Aberdeen Proving Ground (MD): Army Research Laboratory (US); 2013. Report No.: ARL-RP-420.
22. Fresconi F, Celmins I, Silton S, Costello M. High maneuverability projectile flight using low cost components. *Aero Sci Tech*. 2015;41:175–188.
23. Murphy CH. Yaw induction by mass asymmetry. *J Spacecraft Rockets*. 1977;14(8):511–512.
24. Soencksen KP, Newill JF, Plostins P. Aerodynamics of the 120 mm M831A1 projectile: analysis of free flight experimental data. Aberdeen Proving Ground (MD): Army Research Laboratory (US); 2000. Report No.: ARL-TR-2307.
25. Chapman GT, Kirk DB. A method for extracting aerodynamics coefficients from free-flight data. *AIAA J*. 1970;8(4):753–758.

26. Appich WH, McCoy RL, Washington WD. Wind tunnel and flight test drag comparisons for a guided projectile with cruciform tails. Reston (VA): American Institute of Aeronautics and Astronautics; 1980 Jan. AIAA Paper No.: 80-0426.
27. Rogers WK. The transonic free flight range. Aberdeen Proving Ground (MD): Army Research Laboratory (US); 1958. Report No.: BRL-1044.
28. Illiff K. Parameter estimation for flight vehicles. *J Guid Con Dyn*. 1989;12(5):609–622.
29. Klein V, Morelli EA. Aircraft system identification, AIAA Education Series. Reston (VA): American Institute of Aeronautics and Astronautics; 2006. p. 181–221.
30. Nicolaidis JD. A history of ordnance flight dynamics. Reston (VA): American Institute of Aeronautics and Astronautics; 1970 May. AIAA Paper No.: 70-533.
31. Ericsson LE, Reding JP. Steady and unsteady vortex-induced asymmetric loads on slender vehicles. *J Spacecraft Rockets*. 1981;18(2):97–109.
32. DeSpirito, J. CFD aerodynamic characterization of 155-mm projectile at high angles-of-attack. Reston (VA): American Institute of Aeronautics and Astronautics; 2017 Jun. AIAA Paper No.: 2017-3397.
33. Goman M, Khrabrov A. State-space representation of aerodynamic characteristics of an aircraft at high angles of attack. *J Aircraft*. 1994;31(5):1109–1115.

1 (PDF)	DEFENSE TECHNICAL INFORMATION CTR DTIC OCA	C MILLER P MULLER B NELSON B TOPPER	
2 (PDF)	DIRECTOR US ARMY RSRCH LAB RDRL CIO L IMAL HRA MAIL & RECORDS MGMT	RDRL WML G J T SOUTH W DRYSDALE M MINNICINO RDRL WML H J F NEWILL T EHLERS E KENNEDY R SUMMERS C MEYER RDRL WMP D H LYON	
1 (PDF)	GOVT PRINTG OFC A MALHOTRA		
47 (PDF)	DIR USARL RDRL WM J S ZABINSKI RDRLWML P J PEREGINO RDRL WML A WF OBERLE III L STROHM RDRL WML B N J TRIVEDI RDRL WML C S A AUBERT RDRL WML D R A BEYER A BRANT J COLBURN P CONROY M NUSCA Z WINGARD RDRL WML E P WEINACHT V A BHAGWANDIN I CELMINS J DESPIRITO L D FAIRFAX F E FRESCONI III J M GARNER G S OBERLIN T PUCKETT J SAHU S I SILTON RDRL WML F M ILG B ALLIK G BROWN E BUKOWSKI B S DAVIS M DON D EVERSON M HAMAOU K HUBBARD B KLINE J MALEY	2 (PDF)	ARO S STANTON M MUNSON
		2 (PDF)	VTD C KRONINGER B GLAZ
		9 (PDF)	RDECOM AMRDEC L AUMAN J DOYLE S DUNBAR R MATHUR V OVERSTREET B GRANTHAM M MCDANIEL B MCINTOSH C ROSEMA
		1 (PDF)	RDECOM ECBC D WEBER
		29 (PDF)	RDECOM ARDEC D CARLUCCI J CHEUNG S K CHUNG D L CLER B DEFRANCO M DUCA P FERLAZZO R FULLERTON R GORMAN J C GRAU M HOHIL M HOLLIS R HOOKE M KOENIG A LICHTENBERG SCANLAN E LOGSDON

	M LUCIANO P MAGNOTTI G MALEJKO M MARSH G MINER M PALATHINGAL J ROMANO T RECCHIA B SMITH C STOUT W TOLEDO E VAZQUEZ C WILSON	1 (PDF)	NASA I GREGORY
		1 (PDF)	DRAPER LAB G THOREN
		1 (PDF)	GTRI A LOVAS
2 (PDF)	PEO AMMO C GRASSANO P MANZ	2 (PDF)	ISL S THEODOULIS P WERNERT
		3 (PDF)	DRDC D CORRIVEAU C A RABBATH E GAGNON
2 (PDF)	PM CAS P BURKE M BURKE	4 (PDF)	DSTL M HILL T BIRCH
1 (PDF)	MCOE A WRIGHT	1 (PDF)	DSTO N DUONG
3 (PDF)	ONR P CONOLLY D SIMONS R SULLIVAN	2 (PDF)	GEORGIA INST OF TECH M COSTELLO J ROGERS
4 (PDF)	NSWCDD L STEELMAN K PAMADI MALIN J FRAYSSE	1 (PDF)	ROSE HULMAN INST OF TECH B BURCHETT
2 (PDF)	NAWCWD R SCHULTZ M MURPHREE	1 (PDF)	UNIV OF SOUTH FLORIDA T YUCELEN
5 (PDF)	AFRL T J KLAUSUTIS R MURPHEY C PASILIAO E PASILIAO S TEEL	1 (PDF)	ARROW TECH W HATHAWAY
		6 (PDF)	ATK R DOHRN M HEIBEL S OWENS W JENSEN S UZPEN M WILSON
1 (PDF)	AFOSR EOARD G ABATE	4 (PDF)	BAE B GOODELL P JANKE O QUORTRUP D JUNGQUIST
1 (PDF)	MARCORSYSCOM P FREEMYPERS		
1 (PDF)	DARPA J DUNN	1 (PDF)	GD OTS D DEDMONDS

2 UTAS  
(PDF) P FRANZ  
S ROUEN

2 LMMFC  
(PDF) G KANGA  
D PICKEREL

2 RMS  
(PDF) D STRASSMAN  
S WITHERSPOON

1 STA  
(PDF) D MAURIZI

INTENTIONALLY LEFT BLANK.